

MedCLIP-SAMv2: Towards Universal Text-Driven Medical Image Segmentation

Taha Koleilat, Hojat Asgariandehkordi, Hassan Rivaz *Senior Member, IEEE*, and Yiming Xiao *Senior Member, IEEE*

Abstract— Segmentation of anatomical structures and pathological regions in medical images is essential for modern clinical diagnosis, disease research, and treatment planning. While significant advancements have been made in deep learning-based segmentation techniques, many of these methods still suffer from limitations in data efficiency, generalizability, and interactivity. As a result, developing precise segmentation methods that require fewer labeled datasets remains a critical challenge in medical image analysis. Recently, the introduction of foundation models like CLIP and Segment-Anything-Model (SAM), with robust cross-domain representations, has paved the way for interactive and universal image segmentation. However, further exploration of these models for data-efficient segmentation in medical imaging is still needed and highly relevant. In this paper, we introduce MedCLIP-SAMv2, a novel framework that integrates the CLIP and SAM models to perform segmentation on clinical scans using text prompts, in both zero-shot and weakly supervised settings. Our approach includes fine-tuning the BiomedCLIP model with a new Decoupled Hard Negative Noise Contrastive Estimation (DHN-NCE) loss, and leveraging the Multi-modal Information Bottleneck (M2IB) to create visual prompts for generating segmentation masks from SAM in the zero-shot setting. We also investigate using zero-shot segmentation labels within a weakly supervised paradigm to enhance segmentation quality further. Extensive testing across four diverse segmentation tasks and medical imaging modalities (breast tumor ultrasound, brain tumor MRI, lung X-ray, and lung CT) demonstrates the high accuracy of our proposed framework. Our code is available at <https://github.com/HealthX-Lab/MedCLIP-SAMv2>.

Index Terms— Text-driven Image segmentation, Vision-Language models, Foundation Models, Weakly Supervised Semantic Segmentation

I. INTRODUCTION

WITH the growing availability of radiological technologies, there is an increasing demand for precise and

This work has been submitted to the IEEE for possible publication. Copyright may be transferred without notice, after which this version may no longer be accessible.

Submitted September 2024. This work was supported by the Natural Sciences and Engineering Research Council of Canada (NSERC).

Taha Koleilat, Hojat Asgariandehkordi, and Hassan Rivaz are with the Department of Electrical and Computer Engineering, Concordia University, Montreal, Canada (e-mail: taha.koleilat@concordia.ca, hojat.asgariandehkordi@concordia.ca, hassan.rivaz@concordia.ca).

Yiming Xiao is with the Department of Computer Science and Software Engineering, Concordia University, Montreal, Canada (e-mail: yiming.xiao@concordia.ca).

efficient medical image segmentation to support the study, diagnosis, and treatment of various medical conditions [1]. Deep learning (DL) techniques have emerged as state-of-the-art (SOTA) in this field; however, they face three key challenges that hinder their broader clinical use. First, the scarcity of large, well-annotated datasets presents a major obstacle to DL model development. Second, the lack of interactivity and interpretability undermines trust in these methods. Finally, most medical DL models are trained for specific tasks and contrasts/modalities, limiting their flexibility. While several self-supervised and weakly supervised approaches [2]–[4] have been introduced to improve training efficiency, and explainable AI (XAI) techniques (e.g., uncertainty estimation [5], [6] and saliency maps [7], [8]) are under active investigation, cross-domain generalization remains a major challenge.

Recently, the introduction of foundation models, such as Contrastive Language-Image Pre-Training (CLIP) [9] and Segment Anything Model (SAM) [10] has paved the way for interactive and universal medical image segmentation. Several research groups have adapted CLIP and SAM for radiological tasks, including the development of BiomedCLIP [11] and MedSAM [12], which were pre-trained on vast amounts of biomedical data. However, further advances in parameter fine-tuning methods could enhance the performance of these models in radiology.

As interest in SAM grows, to mitigate its reliance on drawing-based prompts (e.g., point and/or bounding box) for segmentation, which require prior clinical knowledge, recent methods have emerged to fine-tune SAM without prompts [13], [14], generate prompts via Class Activation Maps (CAM) from classification tasks [15]–[17], and refine its output using weak supervision [18]–[20]. While still in its early stages, the use of foundation models for interactive and universal medical image segmentation remains an important area for further exploration. To address these challenges, we introduce MedCLIP-SAMv2, a novel framework that integrates BiomedCLIP [11] and SAM [10] for text-prompt-based interactive and universal medical image segmentation, in both zero-shot and weakly supervised settings. The MedCLIP-SAMv2 framework extends and improves upon our original MedCLIP-SAM framework [21] from MICCAI 2024 by incorporating several updates:

- We explored different saliency map generation techniques, where we replaced gScoreCAM [22] with M2IB [23], which, when combined with our fine-tuning of

BiomedCLIP [11], significantly improved zero-shot segmentation.

- We enhanced weakly supervised segmentation results from the previous framework by training nnUNet [24] using pseudo labels and providing uncertainty estimation via checkpoint ensembling [25].
- The validation was expanded by incorporating an additional Lung CT dataset, thereby covering four key radiology modalities—CT, MRI, ultrasound, and X-ray. This comprehensive testing demonstrates the framework's versatility and robustness across diverse segmentation tasks.
- We investigated advanced text prompt engineering strategies by leveraging LLM reasoning and various ensembling methods, which significantly influence zero-shot segmentation performance.
- Significantly more extensive experiments were conducted for further validation, including testing different SAM backbones and visual prompts. We meticulously evaluate the necessity of each component in our framework and demonstrate the incremental contribution to the overall performance.

The refined MedCLIP-SAMv2 framework is now more accurate, advancing further toward universal text-driven medical image segmentation. Our contributions are threefold: **First**, we propose a new CLIP training/fine-tuning approach called Decoupled Hard Negative Noise Contrastive Estimation (DHN-NCE). **Second**, we introduce a text-driven zero-shot medical segmentation method, combining CLIP and SAM for radiological tasks. **Lastly**, we explore a weakly-supervised strategy to further refine zero-shot segmentation results with uncertainty estimation. Our proposed framework is extensively validated across four distinct segmentation tasks and modalities, including breast tumor segmentation in ultrasound, brain tumor segmentation in MRI, and lung segmentation in chest X-ray and CT.

II. RELATED WORK

A. CLIP in Medical Domain

Several works have utilized CLIP for medical images and texts. Despite being trained on 400 million natural image-text pairs, CLIP's performance suffers on medical tasks. For this reason, works like PubMedCLIP [26] suggested fine-tuning CLIP on a set of PubMed articles for the task of Medical Question-Answering; Zhang *et al.* [11] later showed PubMedCLIP's poor performance on cross-modal retrieval tasks (worse than CLIP). On the other hand, MedCLIP [27] proposed a technique to utilize decoupled images and texts in the training process to augment data while Windsor *et al.* [28] explored different methods of enhancing the performance of vision-language models for medical domain tasks in a limited data setting. Alternatively, Wu *et al.* [29] proposed a method of enhancing the text in medical reports by simplifying the sentence complexity. Moreover, other works like [30] and [31] have utilized CLIP for the task of expert pathology detection and medical report generation. However, notably, almost all mentioned works [27]–[31] only utilized Chest X-ray data for

their proposed methods. BiomedCLIP [11] is by far the most recent work for multi-modal medical data on a large scale, which was shown to be superior for cross-modal retrieval accuracy.

B. Weakly Supervised Semantic Segmentation

Many works have explored weakly supervised paradigms for segmenting distinct regions in natural images. CLIP-ES [32] proposed a purely text-driven approach to producing better pseudo-masks through CLIP's class activation maps instead of training affinity networks, while SAMS [18] later extended the work by making use of the SAM model to produce coarse and fine seeds from image-level labels. Additionally, SG-WSSS [33] studied different methods, including scribbles, points, and bounding boxes to prompt SAM through CAM scores. However, these works may fail to translate well to medical scans, which have different characteristics than natural images. Novel CAM techniques specifically tailored for CLIP models like gScoreCAM [22] and M2IB [23] have emerged with SOTA results for generating multi-modal saliency maps. Specifically, gScoreCAM [22] utilized the top-K channel activations from the text and image encoder layers, leading to better-localized saliency maps. The more recent M2IB [23] reformulates the information bottleneck theory to multi-modal applications, where it was proven to outperform CAM-based, perturbation-based, and attention-based saliency mapping techniques. Additionally, M2IB also demonstrated its potential for medical image applications, where a fine-tuned CLIP model on Chest X-ray datasets was shown to properly highlight regions of abnormalities. Recently, Liu *et al.* [34] focus on improving interpretation of zero-shot medical image diagnosis through engineering relevant text prompts by integrating ChatGPT that outputs relevant descriptions of the radiological abnormality. However, the previous works don't inspect improving medical segmentation through model training.

C. SAM for Medical Imaging Modalities

With the advent of SAM, a myriad of research has been dedicated to adapting it for medical imaging purposes. MedSAM [12] provided a large-scale fine-tuning of SAM on about 1 million medical image-mask pairs and demonstrated superior performance when it comes to multiple segmentation tasks. AutoSAM [35] offered a more efficient approach to fine-tuning SAM on medical images through training the prompt encoder and developing a lightweight deconvolution mask decoder for medical segmentation tasks. Cheng *et al.* [36] found that bounding boxes gave the best results when prompting SAM across 12 different medical segmentation tasks, and Huang *et al.* [20] proposed a pseudo-mask correction framework to enhance noisy labels generated from SAM for medical images that can be used for further fine-tuning. Finally, Gong *et al.* [37] replaced SAM's mask decoder with a 3D convolutional neural network so that volumetric medical images can be supported.

III. METHODS

An overview of the proposed MedCLIP-SAMv2 framework is presented in Fig. 1, which is organized into three distinct stages: BiomedCLIP fine-tuning employing our new DHN-NCE loss, zero-shot segmentation guided by text-prompts, and weakly supervised segmentation for potential label refinement.

A. Efficient BiomedCLIP Fine-Tuning with the DHN-NCE loss

Typically, a CLIP model is trained on large datasets consisting of images and their corresponding text descriptions. The model utilizes both an image encoder and a text encoder to extract features from images and texts, projecting them into vectors of the same dimension, denoted as $\mathbf{I}_{p,i}$ for images and $\mathbf{T}_{p,i}$ for texts. Through contrastive learning, the model learns a shared embedding space, where similar image-text pairs are positioned closer together while dissimilar pairs are pulled further apart. Although BiomedCLIP [11] was trained on medical charts/images and clinical texts, further fine-tuning can significantly enhance its performance on tasks specific to medical imaging. In traditional CLIP training with the InfoNCE loss [38], the *negative-positive-coupling* (*NPC*) effect [39] can reduce learning efficiency, especially with smaller batch sizes. Additionally, for medical images, distinguishing between subtle differences in cases within the same imaging category can be challenging. To address these issues, we propose the Decoupled Hard Negative Noise Contrastive Estimation (DHN-NCE) loss, which 1) combines the InfoNCE loss [38] with hard negative sampling [40], emphasizing “close samples”, and 2) incorporates decoupled contrastive learning [39] by removing the positive term in the denominator, allowing for smaller batch sizes. The resulting DHN-NCE loss function, $\mathcal{L}_{DHN-NCE}$, employs weighting functions ($\mathcal{W}_{\mathbf{I}_{p,i}\mathbf{T}_{p,j}}^{v \rightarrow t}$, $\mathcal{W}_{\mathbf{T}_{p,i}\mathbf{I}_{p,j}}^{t \rightarrow v}$) to increase the penalty for negative samples that are close to the anchor, using image-to-text and text-to-image hardness parameters $\beta_1, \beta_2 \geq 0$. In this context, $t \rightarrow v$ refers to text-to-image, while $v \rightarrow t$ indicates image-to-text.

$$\mathcal{L}^{v \rightarrow t} = - \sum_{i=1}^B \frac{\mathbf{I}_{p,i} \mathbf{T}_{p,i}^\top}{\tau} + \sum_{i=1}^B \log \left(\sum_{j \neq i} e^{\mathbf{I}_{p,i} \mathbf{T}_{p,j}^\top / \tau} \mathcal{W}_{\mathbf{I}_{p,i}\mathbf{T}_{p,j}}^{v \rightarrow t} \right) \quad (1)$$

$$\mathcal{L}^{t \rightarrow v} = - \sum_{i=1}^B \frac{\mathbf{T}_{p,i} \mathbf{I}_{p,i}^\top}{\tau} + \sum_{i=1}^B \log \left(\sum_{j \neq i} e^{\mathbf{T}_{p,i} \mathbf{I}_{p,j}^\top / \tau} \mathcal{W}_{\mathbf{T}_{p,i}\mathbf{I}_{p,j}}^{t \rightarrow v} \right) \quad (2)$$

$$\mathcal{L}_{DHN-NCE} = \mathcal{L}^{v \rightarrow t} + \mathcal{L}^{t \rightarrow v} \quad (3)$$

where B is the batch size, τ is the temperature parameter, and the hardness weighting formulas are as follows:

$$\mathcal{W}_{\mathbf{I}_{p,i}\mathbf{T}_{p,j}}^{v \rightarrow t} = (B-1) \times \frac{e^{\beta_1 \mathbf{I}_{p,i} \mathbf{T}_{p,j} / \tau}}{\sum_{k \neq i} e^{\beta_1 \mathbf{I}_{p,i} \mathbf{T}_{p,k} / \tau}} \quad (4)$$

$$\mathcal{W}_{\mathbf{T}_{p,i}\mathbf{I}_{p,j}}^{t \rightarrow v} = (B-1) \times \frac{e^{\beta_2 \mathbf{T}_{p,i} \mathbf{I}_{p,j} / \tau}}{\sum_{k \neq i} e^{\beta_2 \mathbf{T}_{p,i} \mathbf{I}_{p,k} / \tau}} \quad (5)$$

B. Zero-shot and Weakly Supervised Medical Image Segmentation

In this stage, we utilize the fine-tuned BiomedCLIP with the updated parameters $\theta = \{\theta_{img}, \theta_{text}\}$ as the backbone model for feature extraction from both images and text prompts. The core segmentation process relies on the Multi-modal Information Bottleneck (M2IB) technique, which generates visual saliency maps of the target regions by associating text prompts with image regions.

The zero-shot segmentation pipeline can be described mathematically as follows:

Image and Text Embedding Extraction: Given input medical images \mathbf{I} and their corresponding text prompts \mathbf{T} , the image encoder Φ_{img} and the text encoder Φ_{text} from the fine-tuned BiomedCLIP model are used to extract embeddings:

$$\mathbf{Z}_{img} = \Phi_{img}(\mathbf{I}; \theta_{img}) \quad (6)$$

$$\mathbf{Z}_{text} = \Phi_{text}(\mathbf{T}; \theta_{text}) \quad (7)$$

Saliency Map Generation: The embeddings \mathbf{Z}_{img} and \mathbf{Z}_{text} are then passed through the Multi-modal Information Bottleneck (M2IB) module, which learns to align the image and text modalities by maximizing the mutual information between them while filtering out irrelevant information between the image embedding and the input image. Specifically, the M2IB module produces a continuous visual saliency map \mathbf{S} for the image representing the importance of each pixel concerning the text prompt. This visual saliency map is produced by optimizing the following objective function:

$$\mathbf{S} = MI(\mathbf{Z}_{img}, \mathbf{Z}_{text}; \theta) - \beta \times MI(\mathbf{Z}_{img}, \mathbf{I}; \theta) \quad (8)$$

where MI is the mutual information operation and β is a hyperparameter that balances the trade-off between relevance and compression.

K-means Clustering for Initial Segmentation: To generate discrete pixel-wise labels as an initial coarse segmentation, a post-processing step is applied to the saliency map \mathbf{S} . This includes applying K-means clustering to divide the pixels in \mathbf{S} into two groups: foreground (region of interests) and background:

$$\mathbf{Y}_{kmeans} = \text{Kmeans}(\mathbf{S}; k=2) \quad (9)$$

This separates high-intensity (salient) regions from the background based on pixel intensity in the saliency map to get clusters C . Airing, small, disconnected regions arusing A to refine the coarse segmentation. Specifically, clusters with an area smaller than A are filtered out as follows:

$$\mathbf{Y}_{coarse} = \{c \in C : \text{Area}(c) > A\} \quad (10)$$

Segmentation Refinement via SAM: The initial segmentation is used as input to the Segment Anything Model, which refines the segmentation by taking visual prompts \mathbf{V} (e.g., bounding boxes or points) derived from the post-processed

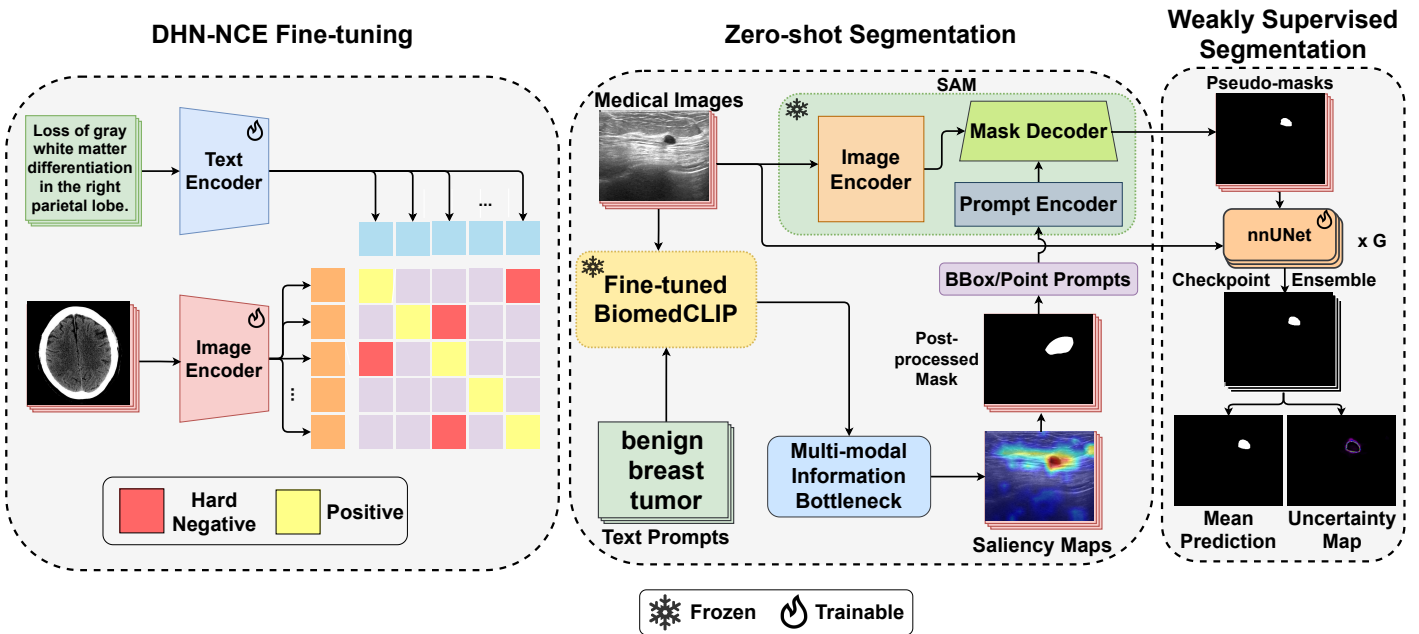


Fig. 1: An overview of the proposed MedCLIP-SAMv2 framework.

clusters. For bounding boxes, we calculate 4 box coordinates (bounding boxes) that enclose each connected contour in the coarse segmentation, while for points, we randomly sample different points that lie within the contour. The final zero-shot segmentation mask $\mathbf{Y}_{\text{zero-shot}}$ is thus produced as:

$$\mathbf{Y}_{\text{zero-shot}} = \text{SAM}(\mathbf{Y}_{\text{coarse}}; \mathbf{V}) \quad (11)$$

Weakly Supervised Training with Pseudo-labels: To further enhance the segmentation accuracy, the zero-shot segmentation results $\mathbf{Y}_{\text{zero-shot}}$ are then used as pseudo-labels with the input medical images \mathbf{I} to train a segmentation network \mathbf{M} in a weakly supervised manner. Thus, the training data will be $\mathcal{T} = \{(\mathbf{I}, \mathbf{Y}_{\text{zero-shot}})\}$. Building on the recent work by Zhao *et al.* [25], checkpoint ensembling has demonstrated superior effectiveness in uncertainty estimation for medical image segmentation when compared to techniques such as Monte Carlo Dropout and mean-field Bayesian Neural Networks. This finding is particularly relevant in the context of the nnUNet framework [24]. Given a total number of epochs E , the training process is divided into D cycles composed of $E_d = \frac{E}{D}$ epochs, and during each cycle, we save G_d checkpoints of the model. After completing all training cycles, the probabilistic prediction of the final segmentation $\mathbf{Y}_{\text{final}}$ is obtained by averaging the predictions from the $G = D * G_d$ total checkpoints saved during the training process providing a Monte-Carlo approximation:

$$p(\mathbf{Y}_{\text{final}}|\mathbf{X}; \mathcal{T}) \approx \frac{1}{G} \sum_{n=1}^G p(\mathbf{Y}_{\text{final}}|\mathbf{X}; \mathbf{M}_n) \quad (12)$$

where \mathbf{M}_n represents the weights of the model at the n -th checkpoint, and \mathbf{X} are unseen testing input images.

Segmentation Uncertainty Estimation: The variation

in predictions across different checkpoints also allows for estimating uncertainty in the final segmentation mask. The generated uncertainty map helps pinpoint regions of the medical scan that exhibit high uncertainty in the prediction. Given R classes in the medical image, the uncertainty for each pixel (i, j) can be computed by calculating the entropy as follows:

$$H(\mathbf{Y}_{\text{final},(i,j)}) = - \sum_{r=1}^R h(r) \log h(r) \quad (13)$$

where

$$h(r) = p(\mathbf{Y}_{\text{final},(i,j)} = r | \mathbf{X}; \mathcal{T}) \quad (14)$$

C. Datasets and Experimental Setup

1) BiomedCLIP fine-tuning: We employed the public MedPix dataset, which contains various radiological modalities, to fine-tune the BiomedCLIP model [11] with our DHN-NCE loss. The base encoders for images and text were the Vision Transformer (ViT) and PubMedBERT [11], respectively. The MedPix dataset was cleaned by removing special characters, trimming leading and trailing white spaces, and excluding samples with captions shorter than 20 characters. All images were resized to 224×224 pixels and normalized according to the RGB channel means and standard deviations used in the original CLIP model [9]. We performed an 85%-15% split, resulting in 20,292 training images and 3,515 validation images. Fine-tuning was performed with a learning rate of 1E-6, a 50% decay rate, and a batch size of 64.

To test the fine-tuning quality of BiomedCLIP, we assessed the top-1 and top-2 accuracy of matching retrievals for both image-to-text and text-to-image on the ROCO (Radiology Objects in COntext) dataset [41], which contains approximately 7,042 multi-modal medical images covering a wide range of radiological cases. We ran the experiments five times with

a batch size of 50, using shuffling to randomize image-text pairs (resulting in 70,420 shuffled examples). In addition, we compared different SOTA loss functions for fine-tuning, including InfoNCE [38], DCL [39] and HN-NCE [42] against our DHN-NCE loss. For a fair comparison, all strategies were trained using the same hyperparameters ($\tau = 0.6$, learning rate = 1E-6), with the hardness parameters for HN-NCE and DHN-NCE set to $\beta_1 = \beta_2 = 0.15$. We also included baseline results from pre-trained BiomedCLIP [11], PMC-CLIP [43], and CLIP [9].

2) Image segmentation accuracy: To evaluate the zero-shot and weakly supervised segmentation results, as well as various design elements of the proposed MedCLIP-SAMv2 framework, we utilized four public datasets, each representing different radiology modalities and tasks. These datasets, which include segmentations of breast tumors, brain tumors, and lungs, were divided into training, validation, and testing sets as follows:

- **Breast Tumor Ultrasound:** The Breast Ultrasound Images dataset (BUSI) [44], containing 600 images of benign and malignant tumors for training. Additionally, 50 and 113 images from the UDIAT dataset [45] were used for validation and testing, respectively.
- **Brain Tumor MRI:** The Brain Tumor dataset [46], comprising 1,462 T1-weighted MRI scans for training, 500 for validation, and 600 for testing.
- **Lung Chest X-ray:** The COVID-19 Radiography Database (COVID-QU-Ex) [47], [48] is divided into 16,280 chest X-rays (normal, lung opacity, viral pneumonia, and COVID-19 cases) for training, 1,372 for validation, and 957 for testing.
- **Lung CT:** CT scans from [49], consisting of segmentation masks for fibrotic diseased lungs from 107 patients, split into 7,959 slices for training, 1,000 for validation, and 1,800 for testing. The split was done by patient ID to prevent data leakage.

For weakly supervised segmentation, we trained the nnUNet [24] architecture for 600 epochs with 3 cycles for all datasets. The learning rate was initialized to 0.01 and we adopted a cyclical learning rate schedule as described in [25], where the learning rate oscillates between a maximum and minimum value throughout each cycle. This allows the model to escape local optima and explore a wider solution space, leading to more diverse and robust predictions. We saved the last 10 checkpoints in each of the 3 cycles resulting in 30 total model checkpoints. The final segmentation result is averaged from the predictions of these 30 checkpoints and is later thresholded to create a binary mask.

3) Experimental setup and metrics: We performed a comprehensive comparison of segmentation quality using the initial labels derived from post-processed M2IB results, zero-shot pseudo-masks, and weakly supervised outputs on the specified testing datasets. Our zero-shot method was benchmarked against SOTA zero-shot (SaLIP [50] and SAMAug [51]) and few-shot (UniverSeg [52], ProtoSAM [53], and Self-Prompt-SAM [54]) segmentation methods. Additionally, we compare our weakly supervised method with nnUNet [24] trained on pseudo-labels without checkpoint ensembling. As

part of the ablation studies for zero-shot segmentation, we examined: **1)** the impact of fine-tuning BiomedCLIP and the choice of explainable AI (XAI) technique for saliency map generation, **2)** the influence of different text prompts on overall segmentation performance, **3)** the contribution of each model component to the final performance, and **4)** the selection of SAM pre-trained models with various visual prompting strategies. These ablation studies were conducted on the test sets of all four datasets mentioned. In all experiments, Dice-Sørensen Coefficient (DSC) and Normalized Surface Distance (NSD) were used as evaluation metrics. Paired-sample t-tests were also conducted to validate the observed trends, with a p-value of less than 0.05 indicating statistical significance.

IV. RESULTS

A. Comparison with SOTA Methods

Table I shows a comparison of the proposed methods with different SOTA techniques. In general, our method demonstrated superior performance in both zero-shot and weakly supervised settings. In the weakly supervised scenario, our method achieved an average DSC of **82.11** and NSD of **87.33**, significantly outperforming all zero-shot and few-shot SOTA methods across various imaging modalities/tasks ($p < 0.05$), except Lung X-ray. However, the fully supervised methods still offer higher accuracy than those using limited resources. Notably, our zero-shot approach achieved an average DSC of **78.21** and NSD of **82.57**, even surpassing weakly supervised nnUNet trained on pseudo-labels without checkpoint ensembling on average.

B. Cross-modal retrieval accuracy

The accuracy of cross-modal retrieval (text-to-image and image-to-text) for the ROCO dataset [41] is shown in Table II across different losses for fine-tuning BiomedCLIP, with three pre-trained CLIP models as baselines. It can be seen that domain-specific pre-trained models performed better than CLIP, with the larger-scale pretraining offering better retrieval accuracy while the pre-trained BiomedCLIP demonstrating the highest retrieval accuracy among all pre-trained models. Fine-tuning BiomedCLIP further enhanced its performance. Specifically, BiomedCLIP fine-tuned with DHN-NCE reached **84.70%** top-1 and **94.73%** top-2 in image-to-text retrieval, and **85.99%** top-1 and **95.17%** top-2 in text-to-image retrieval, significantly outperforming other loss functions and the baseline models ($p < 0.01$). Additionally, the benefit of fine-tuning BiomedCLIP with our DHN-NCE loss is further validated with improved segmentation quality across different tasks and image modalities in Table IV and Table V.

C. Ablation Experiments

1) Effect of text prompt designs: We conducted a series of experiments to analyze the impact of various text prompt designs on zero-shot segmentation performance. In particular, we compared six different prompt configurations: **P0** and **P1** include the class name of the object to be segmented, while **P2** and **P3** consist of longer, descriptive single prompts, and

Technique	Method	Breast Ultrasound		Brain MRI		Lung X-ray		Lung CT		All	
		DSC ↑	NSD ↑	DSC ↑	NSD ↑	DSC ↑	NSD ↑	DSC ↑	NSD ↑	DSC ↑	NSD ↑
Zero-shot	SaLIP	44.33 _{10.12}	48.62 _{10.25}	47.96 _{9.14}	50.24 _{9.26}	63.14 _{11.34}	66.44 _{11.58}	76.32 _{11.22}	78.46 _{11.35}	57.94 _{10.48}	60.94 _{10.61}
	SAMAUG	56.39 _{10.85}	59.23 _{10.92}	45.71 _{10.34}	48.81 _{11.29}	57.18 _{12.12}	60.08 _{12.34}	44.61 _{10.42}	46.48 _{10.57}	50.97 _{11.89}	53.65 _{12.03}
	Ours	78.42 _{9.32}	82.69 _{9.50}	77.12 _{6.82}	83.18 _{6.70}	76.39 _{2.14}	81.63 _{2.15}	80.92 _{5.51}	82.76 _{5.44}	78.21 _{5.70}	82.57 _{5.55}
Weakly Supervised	nnUNet	73.77 _{14.48}	79.71 _{14.79}	77.16 _{12.17}	85.21 _{12.60}	70.15 _{6.40}	74.10 _{6.59}	82.24 _{5.12}	85.65 _{4.70}	75.83 _{9.54}	81.17 _{9.67}
	Ours	78.87 _{12.29}	84.58 _{12.19}	80.03 _{9.91}	88.25 _{10.04}	80.77 _{4.44}	84.53 _{4.51}	88.78 _{4.43}	91.95 _{4.06}	82.11 _{7.77}	87.33 _{7.70}
One-shot	UniverSeg	40.56 _{5.14}	53.25 _{6.22}	23.81 _{5.45}	35.28 _{6.49}	68.15 _{2.21}	80.09 _{2.16}	54.94 _{8.21}	69.62 _{7.59}	46.87 _{10.83}	59.56 _{11.20}
	ProtoSAM	48.44 _{10.93}	50.24 _{10.84}	45.68 _{15.14}	51.69 _{15.65}	80.75 _{1.40}	85.11 _{1.30}	84.50 _{9.94}	87.62 _{9.72}	64.84 _{13.01}	68.67 _{12.74}
Few-shot (K = 4)	UniverSeg	47.56 _{8.57}	54.25 _{8.71}	53.82 _{10.17}	66.40 _{9.96}	79.25 _{2.10}	84.80 _{1.70}	65.68 _{12.02}	70.56 _{11.67}	61.58 _{11.87}	69.00 _{11.31}
	Self-Prompt-SAM	42.04 _{17.19}	44.30 _{17.64}	46.43 _{15.25}	50.29 _{15.83}	67.97 _{2.89}	71.63 _{2.83}	81.50 _{3.84}	83.40 _{3.77}	59.49 _{13.10}	62.41 _{13.06}
Few-shot (K = 16)	UniverSeg	66.36 _{8.57}	72.22 _{8.30}	62.82 _{7.97}	72.76 _{7.94}	83.44 _{1.54}	87.73 _{1.24}	86.49 _{2.49}	89.96 _{1.94}	74.78 _{7.39}	80.67 _{6.25}
	Self-Prompt-SAM	62.36 _{16.38}	66.01 _{16.92}	52.55 _{15.29}	57.07 _{15.93}	82.49 _{2.50}	86.49 _{2.45}	83.66 _{3.90}	85.49 _{3.84}	70.27 _{11.84}	73.77 _{11.69}
Fully Supervised	nnUNet	82.47 _{10.49}	88.32 _{10.77}	87.74 _{6.28}	95.10 _{6.28}	98.72 _{0.65}	99.51 _{0.41}	97.10 _{2.74}	99.18 _{2.13}	84.63 _{5.04}	90.42 _{4.80}
	nnUNet Ensemble	84.72 _{10.97}	90.85 _{11.26}	88.82 _{5.93}	95.84 _{5.54}	99.14 _{2.50}	99.82 _{1.93}	98.12 _{4.09}	99.65 _{4.03}	85.43 _{5.87}	91.74 _{5.71}

TABLE I: Comparison of DSC and NSD values (%) with different few-shot and zero-shot medical image segmentation methods (mean_{std})

Model	Version	image → text (%)		text → image (%)	
		Top-1	Top-2	Top-1	Top-2
CLIP [9]	Pre-trained	26.68 _{0.30}	41.80 _{0.19}	26.17 _{0.20}	41.13 _{0.20}
PMC-CLIP [43]	Pre-trained	75.47 _{0.37}	87.46 _{0.11}	76.78 _{0.11}	88.35 _{0.19}
BiomedCLIP [11]	Pre-trained	81.83 _{0.20}	92.79 _{0.13}	81.36 _{0.48}	92.27 _{0.14}
	InfoNCE [38]	84.21 _{0.35}	94.47 _{0.19}	85.73 _{0.19}	94.99 _{0.16}
	DCL [39]	84.44 _{0.37}	94.68 _{0.19}	85.89 _{0.16}	95.09 _{0.19}
	HN-NCE [42]	84.33 _{0.35}	94.60 _{0.19}	85.80 _{0.17}	95.10 _{0.19}
	DHN-NCE	84.70 _{0.33}	94.73 _{0.16}	85.99 _{0.19}	95.17 _{0.19}

TABLE II: Top-K cross-modal retrieval accuracy (mean_{std}) for CLIP models.

finally **P4** and **P5** are ensembles of 20 text prompts. Note that **P0**, **P2**, and **P4** are generic text prompts, while **P1**, **P3**, and **P5** are more nuanced with subtypes of the target object of interests. For example, for Breast Ultrasound, **P0** is “*breast tumor*” while **P1** can either be “*malignant breast tumor*” or “*benign breast tumor*” depending on the tumor class. For **P2**, we used one descriptive sentence, such as “*A medical breast mammogram showing a suspicious, irregularly shaped mass suggestive of a breast tumor.*” **P3**, on the other hand, includes descriptive text about a specific tumor subtype, like “*A medical breast mammogram showing an irregularly shaped, spiculated mass suggestive of a malignant breast tumor.*” **P4** and **P5** are similar to **P2** and **P3**, but they use an ensemble approach by averaging the text embeddings of 20 different prompts. Here, all descriptive clinical prompts are generated using GPT-4 [55]. For Lung CT, we evaluated solely on generic prompts as there is only one class available. As shown in Table III, the choice of text prompt significantly influences segmentation performance. Class-specific prompts (**P3**) generally yielded

better results for smaller structures like breast and brain tumors whereas generic prompts (**P0**, **P2**) performed better for larger structures like lungs in X-ray and CT scans, where simpler, more generic descriptions allowed the model to focus on larger areas. The best prompt configuration for each task is used to generate the results presented in Table I.

2) Component Ablation Analysis: Table IV shows the contribution of each component of our framework in improving the average segmentation performance on all datasets. Starting with saliency maps generated using the M2IB, we achieved a baseline DSC of **46.23** and an NSD of **50.50**, providing an initial focus on key regions of interest. Fine-tuning BiomedCLIP with the proposed DHN-NCE loss raised the DSC to **49.43** and the NSD to **53.54**. Post-processing the saliency maps with k-means clustering further enhanced the segmentation quality, allowing the model to better delineate foreground and background areas by refining the initial segmentation boundaries. Incorporating a filtering step greatly impacted the results, increasing the DSC to **58.80** and the NSD to **63.10**,

Prompt	Breast Ultrasound		Brain MRI		Lung X-ray		Lung CT	
	DSC ↑	NSD ↑						
P0	65.04 _{15.84}	69.38 _{16.14}	72.00 _{8.47}	77.78 _{8.48}	76.39 _{2.14}	81.63 _{2.15}	71.14 _{6.02}	73.17 _{5.95}
P1	68.88 _{15.03}	73.02 _{15.39}	38.68 _{11.83}	41.37 _{12.33}	71.03 _{5.31}	75.07 _{5.33}	-	-
P2	70.26 _{12.98}	74.60 _{13.35}	72.51 _{7.92}	78.51 _{7.85}	65.23 _{5.54}	69.08 _{5.68}	80.92 _{5.51}	82.76 _{5.44}
P3	78.42 _{9.32}	82.69 _{9.50}	77.12 _{6.82}	83.18 _{6.70}	65.35 _{5.45}	69.29 _{5.55}	-	-
P4	68.86 _{17.18}	72.31 _{17.67}	70.46 _{9.04}	75.69 _{9.25}	70.22 _{5.46}	74.07 _{5.53}	77.38 _{5.76}	79.19 _{5.66}
P5	66.41 _{18.18}	69.99 _{18.71}	71.06 _{8.68}	76.46 _{8.73}	69.82 _{5.31}	73.78 _{5.39}	-	-

TABLE III: Effect of different text prompt templates on the segmentation performance (mean_{std})

as it eliminated small, irrelevant clusters and reduced noise, improving overall precision. With the integration of SAM and the use of visual prompts, such as bounding boxes or points, our zero-shot method yielded a substantial improvement, achieving a DSC of **78.21** and an NSD of **82.57**. Finally, weakly supervised training with checkpoint ensembling further refined the segmentation quality by leveraging pseudo-labels generated from the zero-shot method. By using these pseudo-labels to fine-tune a segmentation network, we were able to reach a final DSC of **82.11** and an NSD of **87.33**.

Method	DSC↑	NSD↑
1: Saliency Maps	46.23 _{6.58}	50.50 _{6.86}
2: + DHN-NCE Fine-tuning	49.10 _{5.46}	53.54 _{5.62}
3: + K-Means Post-processing	52.14 _{4.27}	55.89 _{4.40}
4: + Area-based Filtering	58.80 _{4.73}	63.10 _{4.95}
5: + SAM	78.21 _{5.70}	82.57 _{5.55}
6: + nnUNet Ensemble	82.11 _{7.77}	87.33 _{7.70}

TABLE IV: Effect of different components (mean_{std})

3) Effect of Saliency Maps: As shown in Table V, M2IB achieved the highest performance across all tasks, with an average DSC of **78.21** and NSD of **82.57** when using the fine-tuned BiomedCLIP model. In both its pre-trained and fine-tuned forms, M2IB significantly outperformed gScoreCAM and GradCAM ($p < 0.05$). BiomedCLIP fine-tuning improved the scores across all saliency map techniques on average, with the largest gains seen in M2IB, which improved by **3.98** in DSC and **4.10** in NSD compared to its pre-trained version.

4) SAM and Visual Prompting Comparison: Table VI compares different SAM models and visual prompting techniques. We see that bounding boxes generally provided the best segmentation performance, except in Lung X-rays, where adding point prompts enhanced results. On the other hand, point prompts alone performed worse while combining points and bounding boxes slightly improved the results in some tasks, such as Lung X-ray (**76.22** DSC, **81.30** NSD). In addition, the comparison of SAM, MedSAM, and SAM-Med2D demonstrates that SAM, despite not being pre-trained on medical data, performs well with bounding box prompts,

Model	Technique	All	
		DSC ↑	NSD ↑
Pre-trained BiomedCLIP	M2IB	74.23 _{6.14}	78.47 _{6.02}
	gScoreCAM	59.86 _{6.02}	62.96 _{5.86}
	GradCAM	28.78 _{8.59}	31.87 _{8.34}
Fine-tuned BiomedCLIP	M2IB	78.21 _{5.70}	82.57 _{5.55}
	gScoreCAM	61.73 _{6.22}	64.99 _{6.09}
	GradCAM	30.60 _{8.90}	33.81 _{8.73}

TABLE V: Comparison between different Saliency Map techniques as well as the pre-trained and fine-tuned BiomedCLIP on the overall performance (mean_{std})

achieving high scores in most modalities/tasks, including Lung CT. SAM-Med2D excels in fine-scaled segmentation, but struggles with larger structures, like lung lobes, where MedSAM performs better. The superior performance of SAM may be attributed to its use of a larger model architecture (ViT-H) compared to MedSAM and SAM-Med2D, which only offer ViT-B configurations.

D. Qualitative Segmentation Results

Lastly, we present qualitative segmentation results across the four imaging modalities evaluated in Fig. 2. Our proposed MedCLIP-SAMv2 consistently produced high-quality segmentation masks in weakly supervised settings. For all datasets except Brain MRI, the initial coarse segmentation was suboptimal. However, it provided a sufficient starting point for the zero-shot approach to refine coarse activation maps. For breast and brain tumors, the zero-shot results were notably better than those for Lung CT and Lung X-ray. In Lung CT, the primary challenge for the algorithm was distinguishing between the two lobes. The post-processed results showed one large, connected contour in the center. The zero-shot refinement slightly separated these two regions, though some artifacts persisted. However, the weakly supervised training effectively corrected these false activations, producing a high-quality segmentation map. For Lung X-ray, while the weakly supervised training improved upon the less precise zero-shot

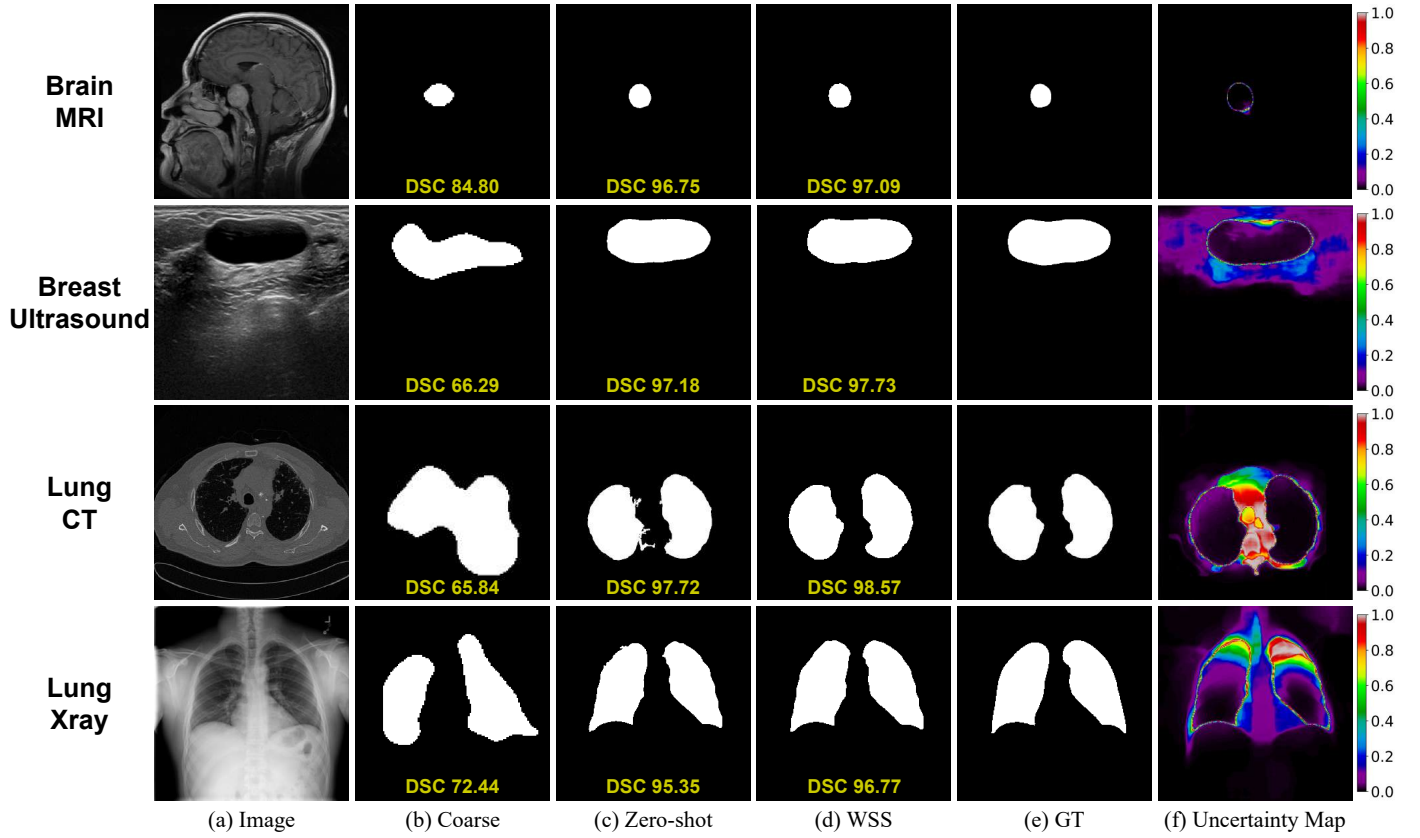


Fig. 2: Qualitative comparison of segmentation results. Coarse=K-means post-processed saliency map, WSS=Weakly Supervised Segmentation and GT=Ground Truth. The uncertainty map corresponds to the weakly supervised segmentation.

Model	Type	Prompts	Breast Ultrasound		Brain MRI		Lung X-ray		Lung CT	
			DSC \uparrow	NSD \uparrow						
SAM	ViT-H	Points	66.30 _{5.76}	69.85 _{5.90}	66.90 _{4.69}	71.92 _{4.83}	76.39 _{2.14}	81.63 _{2.15}	62.11 _{5.25}	64.63 _{5.28}
		BBoxes	78.42 _{9.32}	82.69 _{9.50}	77.12 _{6.82}	83.18 _{6.70}	72.40 _{4.72}	76.38 _{4.76}	80.92 _{5.51}	82.76 _{5.44}
		Points + BBoxes	75.64 _{5.57}	79.60 _{5.62}	76.04 _{3.66}	81.76 _{3.64}	76.22 _{1.94}	81.30 _{1.93}	63.84 _{4.72}	66.23 _{4.71}
SAM-Med2D	ViT-B	Points	74.52 _{5.32}	79.36 _{6.45}	68.68 _{4.21}	77.67 _{3.87}	61.70 _{6.14}	69.28 _{5.91}	67.40 _{4.75}	74.08 _{6.33}
		BBoxes	76.20 _{4.89}	81.46 _{5.74}	56.00 _{3.67}	65.48 _{6.58}	31.60 _{3.92}	37.75 _{4.01}	64.82 _{5.43}	69.80 _{6.27}
		Points + BBoxes	75.96 _{5.11}	80.59 _{3.86}	69.03 _{4.32}	78.06 _{6.02}	38.97 _{5.38}	46.67 _{6.49}	72.70 _{5.07}	79.75 _{4.73}
MedSAM	ViT-B	BBoxes	65.18 _{9.45}	69.22 _{9.51}	68.91 _{7.54}	75.12 _{7.60}	74.30 _{4.94}	77.81 _{4.82}	63.69 _{7.40}	66.10 _{7.28}

TABLE VI: Comparison between different SAM pre-trained models and visual prompting techniques (mean_{std})

masks, the improvement was not as substantial as with Lung CT. Furthermore, we also included uncertainty maps for all predictions. For Brain MRI, high uncertainty was observed only at the edges of the segmentation, which is typical. For Breast Ultrasound, high uncertainty was observed at the borders of the segmentation, while the surrounding area outside the borders showed low uncertainty. In contrast, for Lung X-rays, slight uncertainty appeared in the center of the mask, increasing towards the edges. In the case of Lung CT, high uncertainty was observed both at the edges and in the center of the lung lobes. This was largely due to the artifacts present in the zero-shot pseudo-labels.

V. DISCUSSION

The presented MedCLIP-SAMv2 framework demonstrates superior performance in zero-shot and weakly supervised medical image segmentation tasks across four critical medical imaging modalities: CT, MRI, Ultrasound, and X-ray. By leveraging BiomedCLIP and SAM with visual and text prompts, our method exhibits robust generalization, excelling in complex tasks such as brain and breast tumor segmentation, where smaller and intricate anatomical details pose challenges. This approach notably surpasses other SOTA zero-shot and few-shot methods, especially in difficult segmentation scenarios (see Table I). Recent methods like [56] have demonstrated the potential of CLIP for zero-shot segmentation by

decoupling the pixel-level and image-level classification tasks. However, such methods require fully supervised segmentation ground truth, limiting their application in settings where labels are scarce or noisy. In contrast, MedCLIP-SAMv2 bypasses this requirement and operates without relying on segmentation labels during training, offering a more scalable approach for medical imaging, particularly in weakly supervised settings.

One of the key strengths of our framework lies in the integration of the novel M2IB, which effectively extracts meaningful information from medical images and texts, enhancing segmentation performance. The introduction of the DHN-NCE loss played a crucial role in fine-tuning BiomedCLIP, enabling the model to focus on challenging details while maintaining high performance across all tasks and modalities. Importantly, the combination of M2IB and DHN-NCE allowed the model to generate coarse segmentation masks that are later refined via SAM in a zero-shot setting, proving the versatility of the method without the need for ground truth annotations. The effectiveness of prompt design was another critical insight. Contextually rich, descriptive prompts yielded better results in complex tasks like tumor segmentation, where finer anatomical understanding is required. Conversely, more generic prompts sufficed for simpler tasks like lung segmentation, where larger, distinct structures allowed the model to achieve strong performance with less specific guidance.

Our framework's ability to operate in a weakly supervised paradigm further strengthens its potential clinical applicability. By using pseudo-labels from zero-shot segmentation to fine-tune the model, we saw notable improvements, particularly in lung CT segmentation, where the combination of zero-shot labels and weak supervision generated significant accuracy gains. To the best of our knowledge, we are the first to integrate uncertainty estimation through nnUNet with checkpoint ensembling by training on pseudo-segmentation data, providing a robust method for enhancing segmentation quality while offering insights into prediction confidence. Uncertainty measures are essential in clinical adoption, as they help identify regions where the model's predictions are less certain, enabling clinicians to focus on areas that may require further examination or validation.

Despite the original SAM model not being pre-trained on medical images, it showed strong performance in zero-shot settings, outperforming MedSAM and SAM-Med2D when provided with imperfect visual prompts like points or bounding boxes. This underscores the robustness of SAM to sub-optimal input conditions. Specifically, this can be seen in Fig. 2 where even suboptimal coarse segmentations can be refined using both zero-shot and weakly supervised methods. Looking ahead, future work will focus on extending our framework to handle 3D medical data, a crucial step in advancing the segmentation of volumetric imaging modalities like MRI and CT. Incorporating 3D models will enable our framework to better capture complex anatomical structures, further enhancing its clinical utility. Overall, our findings show that MedCLIP-SAMv2, with its novel integrated components, marks a significant step forward in the development of universal, interactive medical image segmentation. The framework's adaptability across different tasks and its ability to operate

with minimal labeled data emphasize its potential for clinical adoption, particularly in resource-constrained environments.

VI. CONCLUSIONS

We presented MedCLIP-SAMv2, a refined version of the original MedCLIP-SAM framework, improving segmentation performance with minimal supervision across CT, X-ray, Ultrasound, and MRI. By introducing the novel DHN-NCE loss for fine-tuning BiomedCLIP and leveraging SAM, our model achieved enhanced accuracy, particularly in complex tasks. MedCLIP-SAMv2 outperforms its predecessor through superior generalization and refined segmentation, demonstrating strong potential for clinical use in data-limited environments.

ACKNOWLEDGMENT

We acknowledge the support of the Natural Sciences and Engineering Research Council of Canada (NSERC).

REFERENCES

- [1] S. Siuly and Y. Zhang, "Medical big data: neurological diseases diagnosis through medical data analysis," *Data Science and Engineering*, vol. 1, pp. 54–64, 2016.
- [2] A. Baevski, A. Babu, W.-N. Hsu, and M. Auli, "Efficient self-supervised learning with contextualized target representations for vision, speech and language," in *International Conference on Machine Learning*, pp. 1416–1429, PMLR, 2023.
- [3] T. Chen, S. Kornblith, K. Swersky, M. Norouzi, and G. E. Hinton, "Big self-supervised models are strong semi-supervised learners," *Advances in neural information processing systems*, vol. 33, pp. 22243–22255, 2020.
- [4] A. Taleb, C. Lippert, T. Klein, and M. Nabi, "Multimodal self-supervised learning for medical image analysis," in *International conference on information processing in medical imaging*, pp. 661–673, Springer, 2021.
- [5] A. Loquercio, M. Segu, and D. Scaramuzza, "A general framework for uncertainty estimation in deep learning," *IEEE Robotics and Automation Letters*, vol. 5, no. 2, pp. 3153–3160, 2020.
- [6] J. Liu, Z. Lin, S. Padhy, D. Tran, T. Bedrax Weiss, and B. Lakshminarayanan, "Simple and principled uncertainty estimation with deterministic deep learning via distance awareness," *Advances in Neural Information Processing Systems*, vol. 33, pp. 7498–7512, 2020.
- [7] N. Arun, N. Gaw, P. Singh, K. Chang, M. Aggarwal, B. Chen, K. Hoebel, S. Gupta, J. Patel, M. Gidwani, J. Adebayo, M. D. Li, and J. Kalpathy-Cramer, "Assessing the (un)trustworthiness of saliency maps for localizing abnormalities in medical imaging," 2021.
- [8] W. Bae, J. Noh, and G. Kim, "Rethinking class activation mapping for weakly supervised object localization," in *Computer Vision–ECCV 2020: 16th European Conference, Glasgow, UK, August 23–28, 2020, Proceedings, Part XV 16*, pp. 618–634, Springer, 2020.
- [9] A. Radford, J. W. Kim, C. Hallacy, A. Ramesh, G. Goh, S. Agarwal, G. Sastry, A. Askell, P. Mishkin, J. Clark, G. Krueger, and I. Sutskever, "Learning transferable visual models from natural language supervision," 2021.
- [10] A. Kirillov, E. Mintun, N. Ravi, H. Mao, C. Rolland, L. Gustafson, T. Xiao, S. Whitehead, A. C. Berg, W.-Y. Lo, P. Dollár, and R. Girshick, "Segment anything," 2023.
- [11] S. Zhang, Y. Xu, N. Usuyama, J. Bagga, R. Tinn, S. Preston, R. Rao, M. Wei, N. Valluri, C. Wong, M. P. Lungren, T. Naumann, and H. Poon, "Large-scale domain-specific pretraining for biomedical vision-language processing," 2023.
- [12] J. Ma and B. Wang, "Segment anything in medical images," *ArXiv*, vol. abs/2304.12306, 2023.
- [13] Z. Chen, Q. Xu, X. Liu, and Y. Yuan, "Un-sam: Universal prompt-free segmentation for generalized nuclei images," 2024.
- [14] X. Hu, X. Xu, and Y. Shi, "How to efficiently adapt large segmentation model(sam) to medical images," 2023.
- [15] S. Li, J. Cao, P. Ye, Y. Ding, C. Tu, and T. Chen, "Clipsam: Clip and sam collaboration for zero-shot anomaly segmentation," 2024.

[16] Y. Li, H. Wang, Y. Duan, and X. Li, "Clip surgery for better explainability with enhancement in open-vocabulary tasks," 2023.

[17] X. Liu and X. Huang, "Weakly supervised salient object detection via bounding-box annotation and sam model," *Electronic Research Archive*, vol. 32, no. 3, pp. 1624–1645, 2024.

[18] X. Yang and X. Gong, "Foundation model assisted weakly supervised semantic segmentation," 2023.

[19] T. Chen, Z. Mai, R. Li, and W. Jun Chao, "Segment anything model (sam) enhanced pseudo labels for weakly supervised semantic segmentation," 2023.

[20] Z. Huang, H. Liu, H. Zhang, X. Li, H. Liu, F. Xing, A. Laine, E. Angelini, C. Hendon, and Y. Gan, "Push the boundary of sam: A pseudo-label correction framework for medical segmentation," 2023.

[21] T. Koleilat, H. Asgariandehkordi, H. Rivaz, and Y. Xiao, "Medclip-sam: Bridging text and image towards universal medical image segmentation," 2024.

[22] P. Chen, Q. Li, S. Biaz, T. Bui, and A. Nguyen, "gscorecam: What is clip looking at?," in *Proceedings of the Asian Conference on Computer Vision (ACCV)*, 2022.

[23] Y. Wang, T. G. J. Rudner, and A. G. Wilson, "Visual explanations of image-text representations via multi-modal information bottleneck attribution," 2024.

[24] F. Isensee, P. F. Jaeger, S. A. Kohl, J. Petersen, and K. H. Maier-Hein, "nnu-net: a self-configuring method for deep learning-based biomedical image segmentation," *Nature methods*, vol. 18, no. 2, pp. 203–211, 2021.

[25] Y. Zhao, C. Yang, A. Schweidtmann, and Q. Tao, "Efficient bayesian uncertainty estimation for nnu-net," in *International Conference on Medical Image Computing and Computer-Assisted Intervention*, pp. 535–544, Springer, 2022.

[26] S. Esfandi, C. Meinel, and G. de Melo, "PubMedCLIP: How much does CLIP benefit visual question answering in the medical domain?," in *Findings of the Association for Computational Linguistics: EACL 2023* (A. Vlachos and I. Augenstein, eds.), (Dubrovnik, Croatia), pp. 1181–1193, Association for Computational Linguistics, May 2023.

[27] Z. Wang, Z. Wu, D. Agarwal, and J. Sun, "Medclip: Contrastive learning from unpaired medical images and text," 2022.

[28] R. Windsor, A. Jamaludin, T. Kadir, and A. Zisserman, "Vision-language modelling for radiological imaging and reports in the low data regime," 2023.

[29] C. Wu, X. Zhang, Y. Zhang, Y. Wang, and W. Xie, "Medklip: Medical knowledge enhanced language-image pre-training in radiology," 2023.

[30] M. Keicher, K. Zaripova, T. Czempiel, K. Mach, A. Khakzar, and N. Navab, "Flexr: Few-shot classification with language embeddings for structured reporting of chest x-rays," 2023.

[31] E. Tiu, E. Talius, P. Patel, C. P. Langlotz, A. Y. Ng, and P. Rajpurkar, "Expert-level detection of pathologies from unannotated chest x-ray images via self-supervised learning," *Nature Biomedical Engineering*, vol. 6, pp. 1399–1406, Dec 2022.

[32] Y. Lin, M. Chen, W. Wang, B. Wu, K. Li, B. Lin, H. Liu, and X. He, "Clip is also an efficient segmenter: A text-driven approach for weakly supervised semantic segmentation," 2023.

[33] P.-T. Jiang and Y. Yang, "Segment anything is a good pseudo-label generator for weakly supervised semantic segmentation," 2023.

[34] J. Liu, T. Hu, Y. Zhang, X. Gai, Y. Feng, and Z. Liu, "A chatgpt aided explainable framework for zero-shot medical image diagnosis," 2023.

[35] T. Shaharabany, A. Dahan, R. Giryes, and L. Wolf, "Autosam: Adapting sam to medical images by overloading the prompt encoder," *ArXiv*, vol. abs/2306.06370, 2023.

[36] D. Cheng, Z. Qin, Z. Jiang, S. Zhang, Q. Lao, and K. Li, "Sam on medical images: A comprehensive study on three prompt modes," *ArXiv*, vol. abs/2305.00035, 2023.

[37] S. Gong, Y. Zhong, W. Ma, J. Li, Z. Wang, J. Zhang, P.-A. Heng, and Q. Dou, "3dsam-adapter: Holistic adaptation of sam from 2d to 3d for promptable medical image segmentation," 2023.

[38] A. v. d. Oord, Y. Li, and O. Vinyals, "Representation learning with contrastive predictive coding," *arXiv preprint arXiv:1807.03748*, 2018.

[39] C.-H. Yeh, C.-Y. Hong, Y.-C. Hsu, T.-L. Liu, Y. Chen, and Y. LeCun, "Decoupled contrastive learning," 2022.

[40] J. Robinson, C.-Y. Chuang, S. Sra, and S. Jegelka, "Contrastive learning with hard negative samples," 2021.

[41] O. Pelka, S. Koitka, J. Rückert, F. Nensa, and C. Friedrich, "Radiology objects in context (roco): A multimodal image dataset," in *CVII-STENT/LABELS@MICCAI*, 2018.

[42] F. Radenovic, A. Dubey, A. Kadian, T. Mihaylov, S. Vandenbende, Y. Patel, Y. Wen, V. Ramanathan, and D. Mahajan, "Filtering, distillation, and hard negatives for vision-language pre-training," *arXiv:2301.02280*, 2023.

[43] W. Lin, Z. Zhao, X. Zhang, C. Wu, Y. Zhang, Y. Wang, and W. Xie, "Pmc-clip: Contrastive language-image pre-training using biomedical documents," 2023.

[44] W. Al-Dhabayani, M. Gomaa, H. Khaled, and A. Fahmy, "Dataset of breast ultrasound images," *Data in Brief*, vol. 28, p. 104863, 2020.

[45] M. Byra, P. Jarosik, A. Szubert, M. Galperin, H. Ojeda-Fournier, L. Olson, M. O'Boyle, C. Comstock, and M. Andre, "Breast mass segmentation in ultrasound with selective kernel U-Net convolutional neural network," *Biomed Signal Process Control*, vol. 61, June 2020.

[46] J. Cheng, "brain tumor dataset," 4 2017.

[47] M. E. H. Chowdhury, T. Rahman, A. Khandakar, R. Mazhar, M. A. Kadir, Z. B. Mahbub, K. R. Islam, M. S. Khan, A. Iqbal, N. A. Emadi, M. B. I. Reaz, and M. T. Islam, "Can ai help in screening viral and covid-19 pneumonia?," *IEEE Access*, vol. 8, pp. 132665–132676, 2020.

[48] T. Rahman, A. Khandakar, Y. Qiblawey, A. Tahir, S. Kiranyaz, S. B. Abul Kashem, M. T. Islam, S. Al Maadeed, S. M. Zughaier, M. S. Khan, and M. E. Chowdhury, "Exploring the effect of image enhancement techniques on covid-19 detection using chest x-ray images," *Computers in Biology and Medicine*, vol. 132, p. 104319, 2021.

[49] D. Konya, "CT lung & heart & trachea segmentation," Oct. 2020.

[50] S. Aleem, F. Wang, M. Maniparambil, E. Arazo, J. Dietlmeier, G. Silvestre, K. Curran, N. E. O'Connor, and S. Little, "Test-time adaptation with salip: A cascade of sam and clip for zero shot medical image segmentation," 2024.

[51] H. Dai, C. Ma, Z. Yan, Z. Liu, E. Shi, Y. Li, P. Shu, X. Wei, L. Zhao, Z. Wu, F. Zeng, D. Zhu, W. Liu, Q. Li, L. Sun, S. Z. T. Liu, and X. Li, "Samaug: Point prompt augmentation for segment anything model," 2024.

[52] V. I. Butoi, J. J. G. Ortiz, T. Ma, M. R. Sabuncu, J. Guttag, and A. V. Dalca, "Universeg: Universal medical image segmentation," 2023.

[53] L. Ayzenberg, R. Giryes, and H. Greenspan, "Protosam-one shot medical image segmentation with foundational models," *arXiv preprint arXiv:2407.07042*, 2024.

[54] Q. Wu, Y. Zhang, and M. Elbatel, "Self-prompting large vision models for few-shot medical image segmentation," in *MICCAI Workshop on Domain Adaptation and Representation Transfer*, pp. 156–167, Springer, 2023.

[55] J. Achiam, S. Adler, S. Agarwal, L. Ahmad, I. Akkaya, F. L. Aleman, D. Almeida, J. Altenschmidt, S. Altman, S. Anadkat, *et al.*, "Gpt-4 technical report," *arXiv preprint arXiv:2303.08774*, 2023.

[56] J. Ding, N. Xue, G.-S. Xia, and D. Dai, "Decoupling zero-shot semantic segmentation," 2022.